

Investigating the Effects of Air Duct Dimensions on Aeration and Hydrodynamic Characteristics of a Surface-piercing Propeller

Mojtaba Pakian Bushehri¹, Mohammad Reza Golbahar Haghighi¹, Parviz Malekzadeh¹,
Ehsan Bahmyari²

¹ Department of Mechanical Engineering, School of Engineering, Persian Gulf University, Bushehr, 7516913817, Iran,
Email: pakianm@mehr.pgu.ac.ir (M.P.B.); golbahar@pgu.ac.ir (M.R.G.H.); malekzadeh@pgu.ac.ir (P.M.)

² Department of Marine Engineering, School of Engineering, Persian Gulf University, Bushehr, 7516913817, Iran, Email: ehsan.bahmyari@pgu.ac.ir

Received October 20 2023; Revised January 19 2024; Accepted for publication January 25 2024.

Corresponding author: M.R. Golbahar Haghighi (golbahar@pgu.ac.ir)

© 2024 Published by Shahid Chamran University of Ahvaz

Abstract. In this work, considering a propulsion system of a planing boat, the effects of the air ducts with a square cross-section on the thrust, torque, performance, and ventilation of the surface piercing propeller (SPP) are investigated. The fluid flow is simulated using solving of the Reynolds-averaged Navier–Stokes equations (RANS) by the multi-physics computational fluid dynamics software STAR-CCM+. The simulations are validated by studying its grid independency and comparing the numerical results with the extracted results from the sea trial. Then, by considering the actual arrangement of the duct and SPP, the SPP is examined in the open water test in five cases for both condition of the lack and existence of the aeration. Also, the effects of aeration, the advance coefficient and the immersion ratio on the hydrodynamic characteristics of the SPP are studied. In a constant distance between the air duct and propeller, the results show that by increasing the hydraulic diameter of the air duct, the torque and thrust decrease, and the efficiency remains almost constant. Also, it is numerically demonstrated that the effects of the advance coefficient on the torque and thrust coefficients are different for the models with and without aeration.

Keywords: Surface piercing propeller, Aeration, Square air duct, Fully-submerged state, Open water test.

1. Introduction

The surface piercing propellers (SPP) are widely used in propulsion system of the high-speed planing crafts. These propellers usually experience both conditions of the fully-submerged and semi-submerged during the boat's operation. Fig.1 shows the position of the propeller relative to the free surface of water during motion of a planing craft. In the first situation, when the boat is in the pre-planing state, these propellers are fully submerged (Fig. 1(a)) and, in the second state, when the boat is in the post-planing state, these propellers also change their position and become semi-submerged (Fig. 1(b)).

Several experimental studies have been conducted to explore the characteristics of the surface piercing propeller in the earlier last decades of the 20th century ([1-6]). One of the important experimental studies on these types of propellers is the work of Olofsson [7]. He performed a wide range of experimental tests on the propeller model of B-841. With the progress in computer science and computational fluid dynamic methods (CFDs) in recent decades, numerical studies to simulate the behaviors of these propellers have been increased. In this regard, the boundary element method (BEM) and Reynolds-Averaged-Navier-Stokes (RANS)

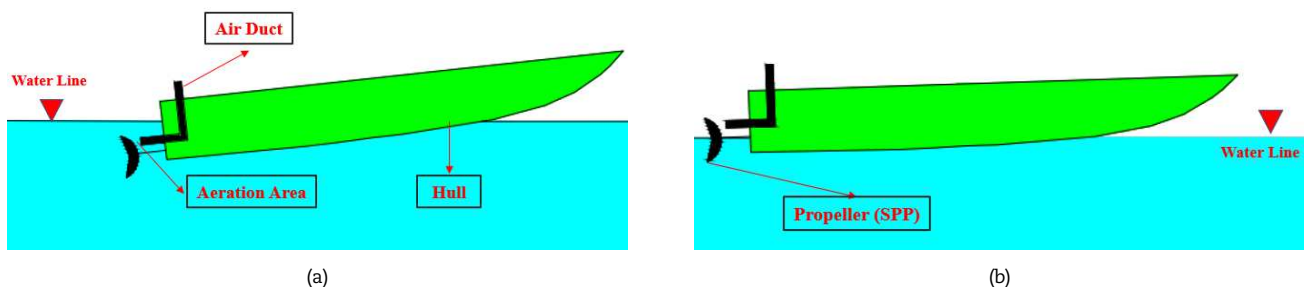


Fig. 1. (a) Pre-planing and fully-submerged states of SPP, (b) post-planing and semi-submerged states of SPP.

equations were employed widely ([8-11]). Caponnetto [12] simulated a surface-piercing propeller using RANS equations and the $k-\epsilon$ turbulence model and validated the results with Olofsson's research. Ghassemi et al. [10] analyzed the three and six-blade surface-piercing propeller using the boundary layer method. Califano and Steen [13] discussed different states for the propeller ventilation at the different immersion ratios (I) by the open water test. They studied the results of complete ventilation under different conditions. Himei [14] analyzed the surface-piercing propeller using the vortex lattice and the RANS equations. They found that the RANS equations agreed with the experimental results. Shi et al. [15] simulated the flow field around a five-blade surface piercing propeller using the RANS equations. Yari and Ghassemi [16] studied partially submerged propellers (PSPs) to achieve a reliable prediction method concerning ventilation around PSPs by employing the RANS-based CFD method. They showed that the ventilation zone shape had a large effect on the results. Alimirzazadeh et al. [17] investigated the impact of immersion ratio on B-841 in different incident angles. Their results revealed that with the increase of the immersion ratio, the torque and thrust coefficient increases, and the efficiency decreases. Yari and Ghassemi [11] studied the ventilation mechanism and forces on B-841 by employing the RANS equations. They showed that the blade cupped phenomenon significantly affects the ventilation pattern, pressure, and force. Javanmardi and Ghadimi [18] studied the hydroelastic properties of a surface-piercing propeller by simultaneously solving the RANS and linear elasticity equations. Ganji Rad et al. [19] studied the 5-blade surface propeller using the sliding mesh technique and employing the volume of the fluid method to simulate the free surface pattern. Nouroozi and Zeraatgar [20] simulated the B-841 propeller by solving the unsteady RANS equations. Seyyedi and Shafaghat [21] investigated the 5-blade surface piercing propeller experimentally. The results showed that by increasing the immersion ratio, the torque and thrust coefficients increase, and the efficiency decreases. Also, Seyyedi and Shafaghat [22] performed a comprehensive review of the experimental, experimental and theoretical, theoretical and numerical studies on the surface piercing propeller. Pakian Bushehri and Golbahar Haghghi [23] investigated the torque, thrust, and efficiency of a surface-piercing propeller mounted on a high-speed marine ambulance boat by sea trial and numerical simulation in the fully-submerged and semi-submerged state under different conditions. Yari and Moghadam [24] studied a surface-piercing propeller with a cup on its blades and compared the torque and thrust coefficients with and without the cup. Kamran et al. [25] investigated the role of the shape of the trailing edge on the performance of a surface-piercing propeller. They found that by suitably choosing the shape of the trailing edge, the thrust and torque coefficients can be increased by about 40%. Seyf and Teimouri [26] studied the scaling effect of the surface-piercing propeller using the RANS equations. They investigated four scales of a surface-piercing propeller for which experimental data were available. Their results showed that the hydrodynamic coefficients were affected by the pressure component induced by the ventilation pattern.

As the above literature review shows, extensive research has been conducted on surface-piercing propellers. Most of these works have investigated the SPP in the semi-submerged state, and some of them have been concerned with both the semi-submerged and fully-submerged states. In the fully-submerged state, to reduce the propeller torque and match the engine torque, the propeller is ventilated by the air duct, as shown in Fig. 1. In most of their applications, the high-speed planing crafts work in the pre-planing state (at boat speed less than planing speed). Therefore, it is essential to study the hydrodynamic characteristics of the surface piercing propellers in the fully-submerged state. In the fully-submerged state, the high torque of the SPP overloads the engine. This means the propeller torque becomes more significant than the engine torque, which causes the engine speed and the ship speed to remain constant in a specific range and cannot increase further [27]. To overcome this problem and reduce the propeller torque, the propeller is ventilated by an air duct located on the suction side of the propeller, and with the propeller rotation, the air is sucked from the free water surface. However, very little research is available on the aeration of surface-piercing propellers. Yang et al. [28] investigated the influence of aeration on the performance of a surface-piercing propeller using an air tube located on the suction side and in line with the propeller hub. In continuation of previous work, Gao et al. [29] studied the effect of aeration on three tube diameters. They showed that after aeration, the torque and thrust decrease, but the efficiency increases only at a high advance coefficient. However, in two studies, the air pipes have been aligned with the propeller hub and do not correspond to the arrangement of the actual propulsion system of a planing boat. Amini et al. [30] experimentally studied the effects of the air tube on the suction side and below the propeller. Their results cleared that by suitably locating the air tube, the thrust coefficient can be improved up to almost 100%. In the previous study, the SPP has been investigated in $I \leq 1$, and the air pipe has been located below the propeller hub and focused on the distance between the air tube and the propeller with force ventilation.

In the present work, the aeration effect on the surface piercing propeller is carried out based on the actual surface propulsion system of a planing boat in the pre-planing state where the SPP is fully-submerged (in the planing boat, aeration to SPP is only required in the fully-submerged state to overcome the engine overload). Contrary to the previous research, according to the studied boat, a square duct is used for aeration, and the air duct is placed on the top of the hub. In addition, the propeller is ventilated by the air duct only in the fully-submerged state for the pre-planing state and deep immersion ratio ($I > 1$), which has not been investigated in the related previous works. This work aims to be a comprehensive study on the aeration of the surface piercing propeller, and the results of this study can be used for the designers of the surface propulsion systems in designing the propeller and choosing the air duct to achieve the planing speed of the high-speed planing craft. In this regard, firstly, the effect of changing the hydraulic diameter of the air duct on the torque, thrust, efficiency, and ventilation of the propeller will be studied and compared with the cases without aeration state. Finally, the effect of changing the advance coefficient and the immersion ratio at the different aeration cases will be investigated.

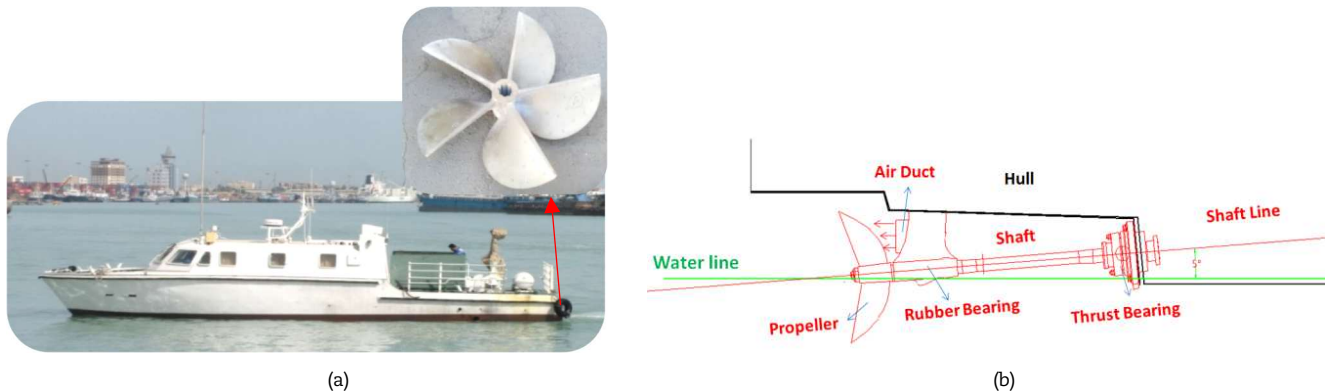


Fig. 2. (a) Planing catamaran boat and its five-blade surface piercing propeller. (b) Shaft line view.



Table 1. Vessel particulars and propeller specification.

Vessel particulars			Propeller specification				
Length	16 (m)	Tunnel Width	1.5 (m)	Diameter	770 (mm)	No. of Blades	5
Width	4.4 (m)	Max Speed	44.5 (Knots)	Pitch	980 (mm)	DAR	75%

2. Boat and Propeller Specification and Simulation Method

2.1. Boat and propeller specification

The hydrodynamic characteristics of a 16-meter catamaran vessel with a five-blade surface-piercing propeller were studied to examine the effect of changing the hydraulic diameter ratio of a SPP. The boat and propeller are shown in Fig. 2(a). The vessel particulars and propeller specifications are detailed in Table 1. Additionally, the shaft line of the boat is illustrated schematically in Fig. 2(b), showing the location of the air duct on the suction side and above the hub. This arrangement causes the propeller to suck air above the free surface and ventilate it when the boat is in the pre-planing state, with the duct lying under the water. In the post-planing state, the air duct emerges from the water, positioning the propeller in a semi-submerged state (see Fig. 1(b) and Fig. 2(b)).

2.2. Governing equations

Based on the previous studies ([12, 14, 15-20, 22-26]), the RANS equations are appropriate to simulate the fluid field around the propellers that work near the free surface. For an incompressible Newtonian fluid, the RANS equations are expressed as:

$$\rho \frac{\partial \bar{U}_i}{\partial t} + \rho \bar{U}_j \frac{\partial \bar{U}_i}{\partial x_j} = \rho \bar{f}_i - \frac{\partial \bar{p}}{\partial x_j} \delta_{ij} + \frac{\partial}{\partial x_j} (2\mu \bar{S}_{ij} - \overline{\rho u_i' u_j'}) \quad (1)$$

where

$$\bar{S}_{ij} = \frac{1}{2} \left(\frac{\partial \bar{U}_i}{\partial x_j} + \frac{\partial \bar{U}_j}{\partial x_i} \right) \quad (2)$$

\bar{U}_i is the average velocity component along the x_i - axis, \bar{p} is the average pressure; ρ , δ_{ij} , μ and t are, the mass density, Kronecker delta, dynamic viscosity and time, respectively; also, \bar{S}_{ij} is the mean strain rate tensor component and u_i' is a varying velocity component along the x_i - axis. The three-dimensional RANS equations and the mass continuity equation result in four independent equations with ten unknown variables. The inequality between the number of equations and unknowns makes it impossible to solve this problem analytically. On the other hand, the presence of Reynolds stresses ($\overline{\rho u_i' u_j'}$) increases its complexity. To solve such a problem, usually, Reynolds stresses are modeled using viscosity models on linear vortices as follows:

$$-\overline{\rho u_i' u_j'} = 2\mu_t \bar{S}_{ij} - \frac{2}{3} \rho k \delta_{ij} - \frac{2}{3} \mu_t \frac{\partial \bar{U}_k}{\partial x_k} \delta_{ij} \quad (3)$$

where μ_t and k are the turbulent viscosity (or vortex viscosity) and the turbulent kinetic energy, respectively. The turbulent viscosity can be estimated using several models. One of these models is to use a two-equation model. In this work, the k - ϵ turbulence model is employed ([11, 12, 14, 16, 31, 32, 33]).

The volume of fraction (VOF) is utilized to simulate the interface of two fluids in the mixing flows. Eq. (4) and Eq. (5) show the distribution of phases in a fluid cell:

$$a_i = \frac{V_i}{V} \quad (4)$$

$$\sum_{i=1}^N a_i = 1, 0 < a_i < 1 \quad (5)$$

where a_i and V_i are, respectively, the volume fraction and the volume of fluid i , V is the cell volume, and N is the number of phases. Consequently, the density and viscosity are determined as, respectively:

$$\rho = \sum_i \rho_i a_i \quad (6)$$

$$\mu = \sum_i \mu_i a_i \quad (7)$$

ρ_i and μ_i are the density and viscosity of phase i , respectively.

The advance coefficient J , torque coefficient K_t , and propeller thrust coefficient K_q are defined as [34]:

$$J = \frac{V}{n_p D}, K_t = \frac{T}{\rho n_p^2 D^4}, K_q = \frac{q}{\rho n_p^2 D^5} \quad (8)$$

2.3. Simulation characteristics

The fluid flow around the propeller is simulated using the computational fluid dynamics-based software STARCCM+ (version 2020.1). Due to many simulations for few case studies, workstation computers equipped with Intel® Core™ i9-9900k CPU @ 3.6GHz have been used in parallel processing mode. To study the fully-submerged state, the propeller is modeled with an air duct and tested in open water conditions in five cases: without aeration and for four air duct hydraulic diameters. First, to validate the numerical solution, the fluid flow around the boat hull and the propeller, and the air in the duct are analyzed, and the results are compared with the sea trial. Since the boat is a catamaran, only a demi hull with a propeller and an air duct is considered. In most of the planing boats, the propellers are installed at an inclining angle. Accordingly, in this study, the propeller with an inclining angle of 5 degrees is tested and the effect of changing the hydraulic diameter ratio of the air duct is carried out. Figure 3 shows the hull model with the propeller and the air duct, and Fig. 4 shows the propeller model and the air duct. The air duct hydraulic diameter D_h , the air duct hydraulic diameter ratio Q_h , and the immersion ratio (I) are calculated as follows, respectively.



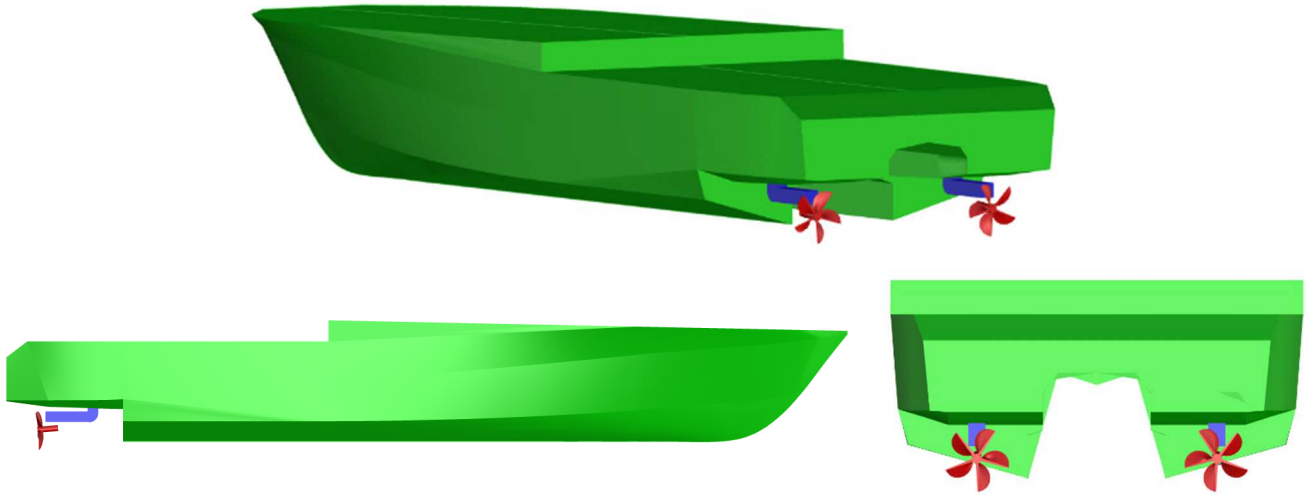


Fig. 3. Model of hull, propeller and air duct.

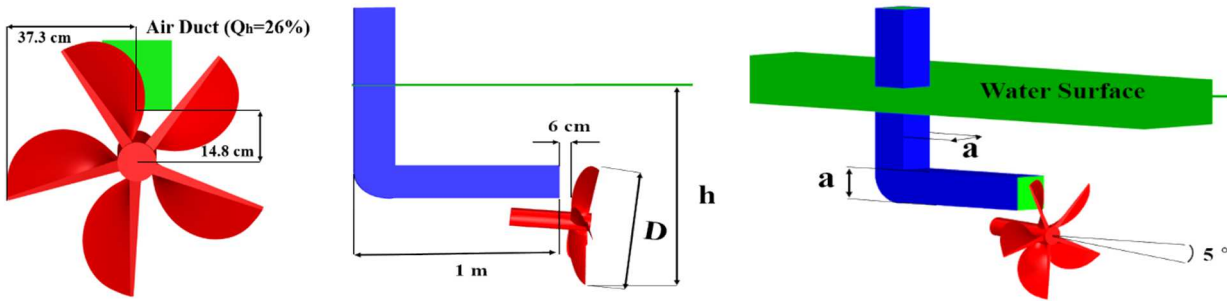


Fig. 4. The propeller and air duct model.

$$Dh = a, Qh = \frac{Dh}{D}, I = \frac{h}{D} \tag{9}$$

In the under-investigation boat, Qh is 26%, and also, in the pre-planing state, the immersion ratio (I) is greater than one. However, the effect of other values of the hydraulic diameter ratio (Qh) are numerically examined.

As it is clear from Fig. 4, the air duct length is considered large, so the air duct wakes have less effect on the ventilation. The air duct location and its distance from the propeller are shown in Fig. 4 for the under-investigation boat. When changing the hydraulic diameter of the air duct in different cases under investigation, the distance of the lower edge of the duct from the propeller center and the duct center from the propeller radius are kept constant, which are 14.8 cm and 37.3 cm, respectively. The geometric dimensions and the corresponding hydraulic diameters of the examined ducts are given in Table 2.

2.4. Numerical simulations

The physical domain of the system is assumed to be in the form of a cylinder. The boundary conditions, the domain dimensions, and the corresponding mesh with and without hull of the model are shown in Figs. 5(a) and 5(b), respectively. For the model without the hull, the diameter and height of the tank computational domain are selected as $8D$ and $13D$, respectively; D is the propeller diameter ([17, 19, 35]). In the present work, the influences of the hull on the input flow velocity of the propeller are investigated without analyzing the forces exerted on the hull.

When simulating the model with the hull, the tank should be large enough to position the hull at sufficient distances from the tank wall. To achieve this, the tank's diameter and length are chosen to be $2L$ and $2.5L$, where L is the boat length and in terms of the propeller diameter (D) become $41.55D$ and $51.94D$, respectively. The boundary conditions are consistent for both models, with and without the hull. The air and water inlet are on the suction side of the propeller, while the outlet is on the pressure side. During the simulation, the propeller's torque and thrust are measured while considering the inclining angle. The simulations are conducted in 5 modes: without aeration and for hydraulic diameter ratios Qh of 13%, 26%, 38%, and 52%, at the advance coefficient of 0.39 and 0.6, and the immersion ratio of 127% and 179% (i.e., $I = 1.27$ and $I = 1.79$, respectively). It is important to noted that in the presented results, $Qh = 0$ indicates the case of without aeration state.

Table 2. Air ducts dimensions and the corresponding hydraulic diameter.

a (m)	Dh (m)	D (m)	Qh
0.1	0.1	0.77	13%
0.2	0.2	0.77	26%
0.3	0.3	0.77	38%
0.4	0.4	0.77	52%



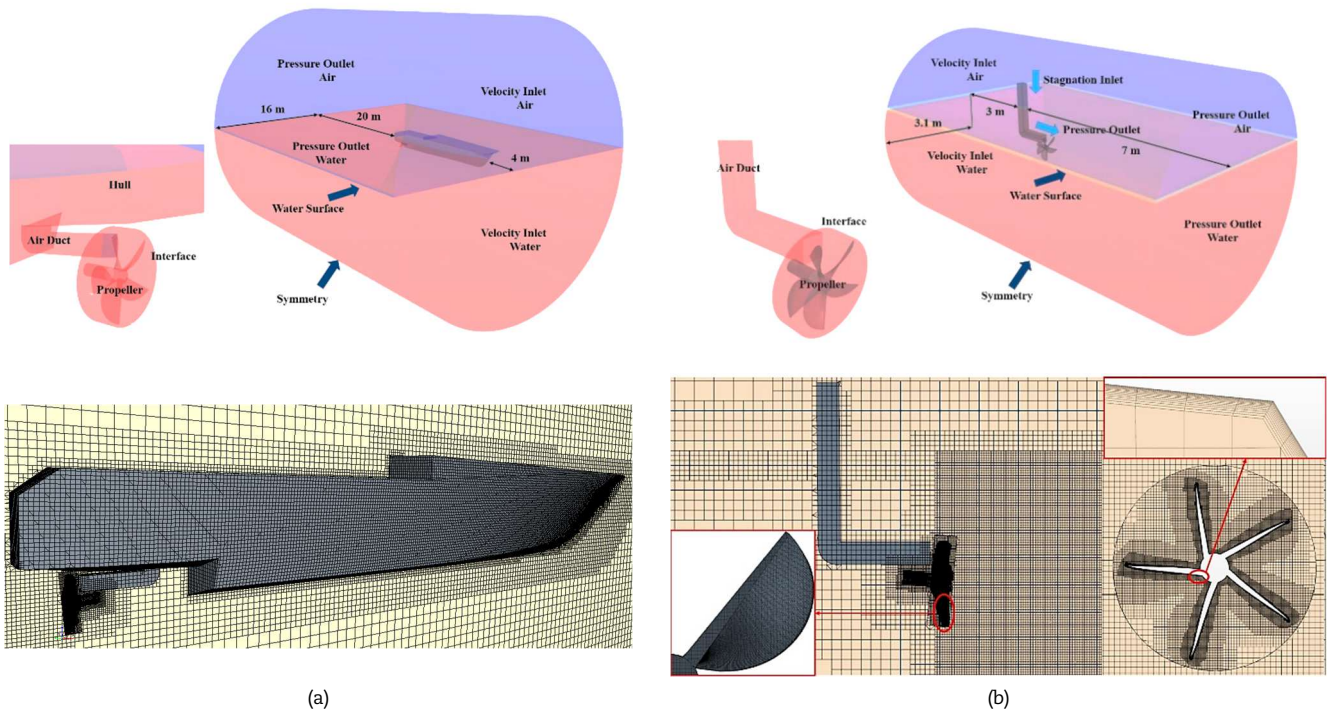


Fig. 5. Boundary conditions, computational domain dimensions and meshing of the model (a) with and (b) without hull.

Three types of meshes are used: trimmer mesh, surface mesh, and prism layer mesh, which have been in the domain, on the surfaces, and the boundary layer, respectively. Also, the sliding mesh is used to simulate the propeller rotation.

The solution setting and used models in STARCCM+ summarized in Table 3.

In simulations, the dimensionless parameter y^+ is evaluated. This parameter indicates the first layer distance of the boundary mesh to the geometry surface. In other words, y^+ is a non-dimensional wall distance parameter that indicates the computational cell position within the different areas of the boundary layer thickness. For all turbulent boundary layers when the y^+ is less than 5, it means that the referred cell is located in the viscous-sublayer. The y^+ is defined as:

$$y^+ = \frac{u^* y}{\nu} \tag{10}$$

where

$$u^* = \sqrt{\frac{\tau_w}{\rho}}, \tau_w = C_f \left(\frac{1}{2} \rho V^2\right) \tag{11 a,b}$$

Here, u^* is frictional velocity, y distance of first mesh from the surface, τ_w wall shear stress, C_f frictional coefficient, and V is the velocity. STARCCM+ user guide provides suggested y^+ values for each turbulent model and wall function. For instance, by using realizable two-layer $k-\epsilon$, which is used in this paper, only the All- y^+ treatment is defined as a wall function. The solver of the turbulent flow used in the STARCCM+ software uses a High- y^+ treatment of wall function for $y^+ > 30$ and a Low- y^+ treatment $y^+ < 5$. In addition, for the buffer zone ($5 < y^+ < 30$) based on the blending function, it calculates suitable values for solving the boundary layer flow [36]. Figure 6 shows the values of y^+ for a blade. The value of y^+ is less than 5 over a large portion of the blade surface area, and it is between 5 and 100 near the leading edges and tip of the blade, and very limited points on the leading edge are in the range of 100 to 140. The calculated value of y^+ indicates the high quality of the grid.

3. Results and Discussion

3.1. Convergence studies

Grid independency is studied for the models with and without the hull and the results of the case without the hull are presented in Table 4. In the case of the model with the hull, the difference between consecutive results becomes less than 2.1% for torque and less than 1.8% for thrust after 9650236 meshes. Therefore, 9650236 meshes are used to generate the results for the model with the hull. For the simulation of the model without the hull, as shown in Table 4, the convergence results are adequate with 4134529 meshes. However, 7345215 meshes are selected to illustrate two-phase flow of $\alpha_i = 0.5$ more desirable.

Table 3. The settings used in the STARCCM+ Software.

Parameter	Method	Descriptions
1 General	Implicit Unsteady, Segregated flow	-
2 Turbulent Model	Turbulent	k-ε turbulence
3 Multiphase	Eulerian Multiphase	Air and Water, Constant density
	Reynolds-Averaged Navier-Stokes	-
4 Solution Method	Volume fraction VOF	Composite Air and Water HRIC



Table 4. Grid independency study.

Number of meshes	Thrust coefficient	Thrust difference	Torque coefficient	Torque difference
1015519	0.203	-	0.0424	-
4134529	0.184	9.46%	0.0391	7.99%
7345215	0.179	2.6%	0.0383	2.2%
11885260	0.175	2.2%	0.0376	1.7%

Table 5. Specification of sea trial in experimental and simulation.

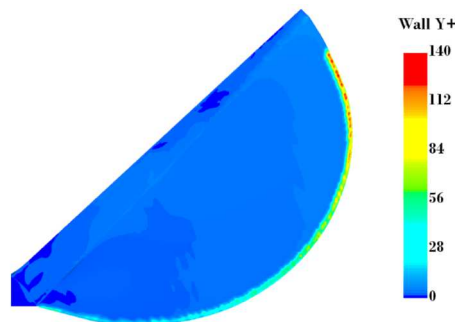
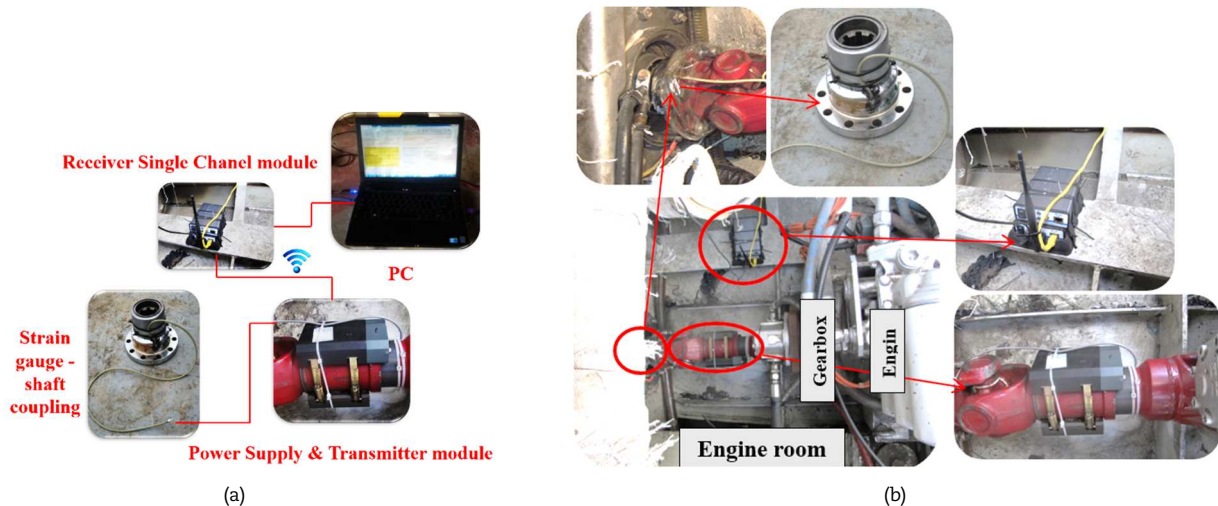
Trial	Vs (Knot)	n_p (rpm)
First trial	7.7	733.33
Second trial	11.6	1060
Third trial	14	1200
Forth trial	16.2	1400

3.2. Validation of numerical simulation

To validate the numerical solution, the sea trial was performed using a torque-measuring device. The propeller torque has been obtained through this device for four ship speed (V_s) and propeller angular velocity (n_{prop}) (see Table 5). Figure 7 shows the schematic of the torque-measuring device and its setup in the engine room of the boat. The torque measurement was done in the engine room of the boat after the propulsion components, such as the thrust bearing and the shaft bracket bearing (see Fig. 2(b) and Fig. 7). The torque is obtained by strain gauge sensors, which is installed on the shaft coupling, and its output after being amplified is transmitted through the wireless communication to the receiver module (transmitter module is installed on the shaft cardan and the receiver module is installed on the structure of engine room). The calibrating and extracting of the gain of the device were explained in the research [23]. Sea trial conditions were conducted in calm sea, and the wind speed was assumed to be 3 km/h. An air duct with a hydraulic diameter ratio of 26% ($a=20$ cm) was used to perform the sea trial. Experimental and simulations of the sea trials were performed for the propeller angular speeds of 733.33, 1060, 1200, and 1400 rpm and the corresponding boat speeds reported in Table 5.

Figure 8 shows the numerical simulation results for the demi-hull in the first sea trial (see Table 5). The air inlet is located on the deck and the boat's stern. The air is sucked by the propeller, and the blades are ventilated. The propeller rotates, and the two-phase flow of water and air is cut by the blades and thrown forward, and then they move towards the free surface. It should be mentioned that in this research, only the hydrodynamic characteristics of the propeller is analyzed, and consideration of the hull in the sea trial simulations is due to its effect on the inlet flow to the propeller. Therefore, the trim is assumed to be zero in four sea trial simulations.

Figure 9 shows the extracted torque in experimental work and simulation for the 1200 rpm angular velocity of the propeller. In the experimental sea trial (Fig. 9(a)), the angular speed is recorded based on the engine sensor, which should be divided by 1.5 (gearbox reduction ratio). Due to oscillation in the torque diagram, the mean values of torques are evaluated by averaging the propeller torques. The averaging is calculated in the simulation after the convergence of the solution (Fig. 9(b)).

**Fig. 6.** The y^+ contour on a blade surface.**Fig. 7.** Experimental setup (a) Schematic of torque measuring device (b) Installation of the torque measuring device in the engine room.

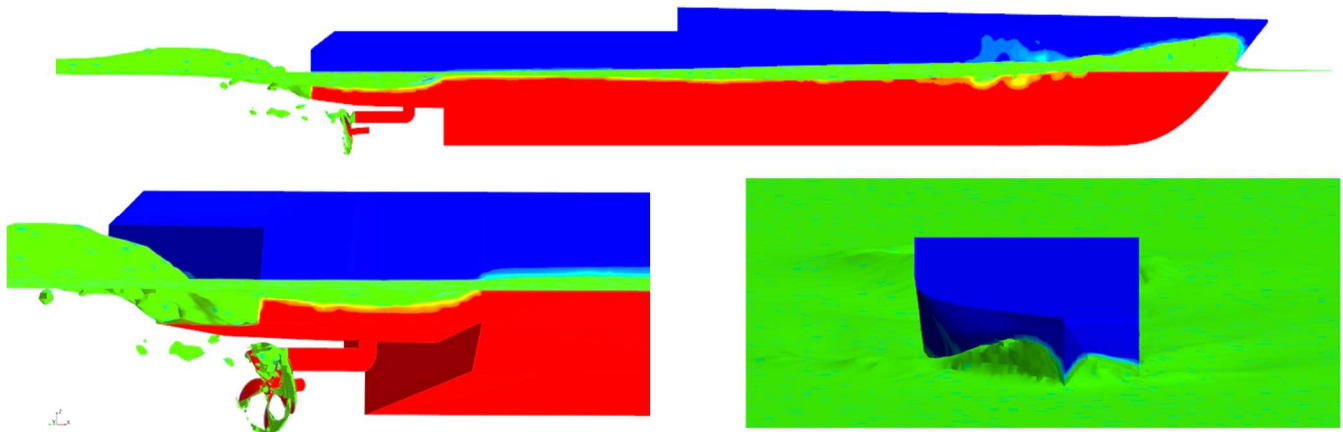


Fig. 8. Simulation of the first sea trial.

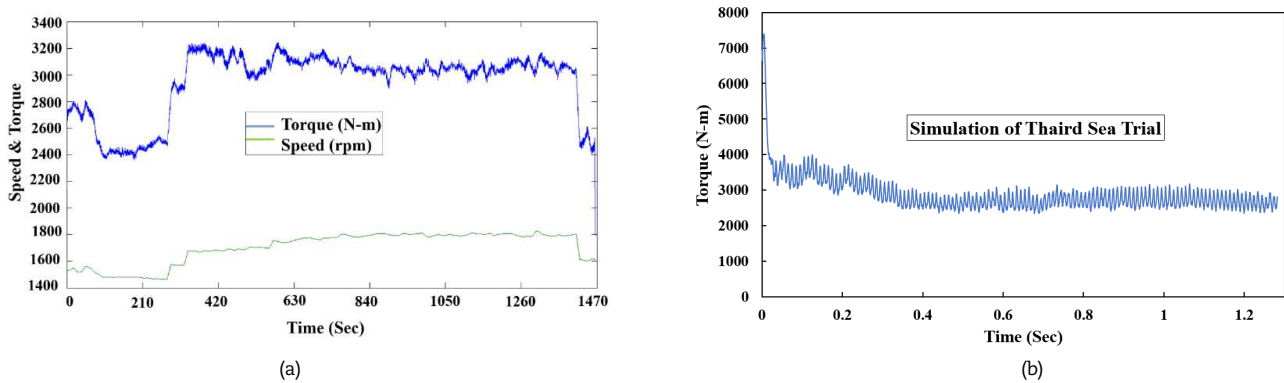


Fig. 9. Extract the torque in the third sea trial (a) Experiment (b) Simulation.

Table 6 shows the comparison of the extracting torque in experimental work and simulation for four sea trials. Some sources of the errors between the results are due to limitations of the numerical simulation in considering some conditions of the sea trial, such as the trim following the ship speed and likely change in the propeller immersion following the sea trial condition, etc. In addition, the difference in the location of the torque measurement in the experimental and the simulation affects the errors, because the friction in the bearings increases the torque in the experimental sea trial.

Also, based on the uncertainty analysis of experimental sea trial, the uncertainty error is estimated to be about 2.1%. This includes the accuracy of sensors, the GPS with 0.1 knot accuracy and the engine speed with about 50 rpm accuracy [23]. So, this uncertainty can contribute to any discrepancies between the experimental and simulation results.

As mentioned previously, the purpose of this study is to investigate the effect of an air duct on the surface piercing propeller in the fully-submerged state. Hence, it is not necessary to consider the hull in numerical simulations, which considerably reduces the run time of the calculations. Thus, the hull is removed in the subsequent simulations and the simulations are performed in open water tests. To investigate the effect of removing the hull on the hydrodynamic characteristics of the propeller, the sea trial simulations were repeated without the hull for two angular speeds, 733.33 rpm and 1200 rpm of the propeller, and the flow velocity is considered as the boat speed. More details of the results for these four simulations are presented in Table 7. From the presented results in Table 7, it can be concluded that the effect of the hull on the torque and thrust has a slight difference for 733.33 rpm. But this difference increases for 1200 rpm. This means that at the high boat speed, the hull causes a significant difference between the inlet and outlet velocity of water to the propeller.

3.3. Results of open water test simulations

After validating the numerical simulation and demonstrating the effect of the hull on torque and thrust, the results from the open water test without the hull are presented in this section. The specifications of open water tests in numerical simulation are provided in Table 8. The numbers 1, 2, 3, 4, and 5 shown in the last column of Table 8 indicate the aeration cases and correspond to the hydraulic diameter ratio of 0, 13%, 26%, 38%, and 52%, respectively. A hydraulic diameter ratio of zero represents the case without aeration.

Since the operation of these propellers in the fully-submerged state is related to the low advance coefficient, the investigations are carried out for the advance coefficients of 0.39 and 0.6. Additionally, two immersion depth ratios of 179% and 127% are considered, corresponding to low and high boat speeds, respectively. The 127% immersion depth ratio is near the post-planing state, placing the propeller close to the free water surface. At the immersion depths of 127% and 179%, the distance from the free water surface to the blade tip is 21 cm and 61 cm, respectively.

Table 6. the comparison of extracting torque between the experimental work and Simulation.

Trial	q in Experiment (N-m)	q in Simulation (N-m)	Error (%)
First trial	1403	1190	15.2
Second trial	2460	2096	14.7
Third trial	3100	2650	14.5
Forth trial	4029	3331	17.3



Table 7. Effect of the hull on the torque and thrust.

Propeller angular speed (rpm)	Average torque with hull (N.m)	Average thrust with hull (N)	Average torque without hull (N.m)	Average thrust without hull (N)	Difference in torque %	Difference in thrust %
733.33	1190	5829	1210	6080	1.6	4.1
1200	2654	13893	2400	12237	9.5	11.9

Table 8. Specification of open water tests in numerical simulation.

$I = h/D$	h (m)	J	n_p (rpm)	Aeration
1.27	0.983	0.39	733.33	1,2,3,4,5
1.27	0.983	0.6	800	1,2,3,4,5
1.79	1.383	0.39	733.33	1,2,3,4,5
1.79	1.383	0.6	800	1,2,3,4,5

Figure 10 shows the torque and thrust diagram in five different aeration cases in one rotation cycle of the propeller for the advance coefficient of 0.39 and the immersion ratio $I = 1.79$. The highest value of the torque and thrust coefficient is associated to the without aeration case, and it is reduced with aeration. The aeration increases by increasing the hydraulic diameter ratio (i.e., Q_h). In all aeration cases, the torque and thrust diagrams have oscillation, and for $Q_h = 13\%$, the variations of the torque and thrust are highly irregular. This behavior is observed in all simulations with $Q_h = 13\%$ due to the small hydraulic diameter of the air duct and the low volume of aeration, which results in irregular contact of the blades with the two-phase flow. Consequently, when the blade passes through the duct front area, a peak is formed in the diagram. So, there are big peaks in the diagram in one the propeller rotation as many as the number of propeller blades. As the hydraulic diameter increases, the peak height of the torque and thrust decrease and the oscillation frequency increases.

Figure 11 shows the changes in the torque diagram according to the passage of the three blades in the front area of the air duct. When the yellow blade is precisely in the front of the air duct, the rotation angle is zero. When the propeller rotates and the yellow blade is changed its position from 0 to 11 degrees, the torque increases. At 11 degrees, when the leading edge of the yellow blade leaves the front area of the air duct, the torque value is maximum.

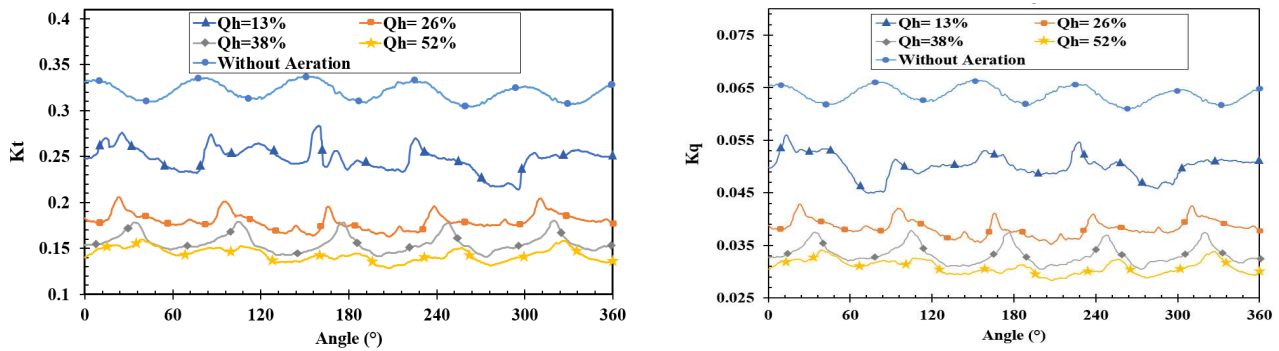
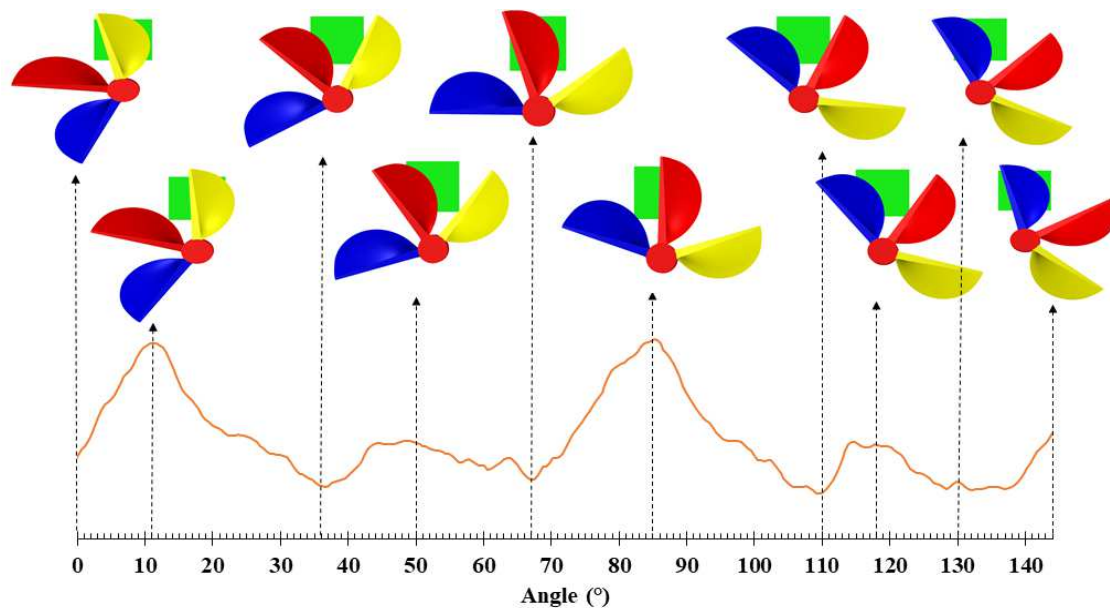
Fig. 10. Compression of torque and thrust coefficients in one rotation of the propeller for $Q_h = 0, 13\%, 26\%, 38\%$ and 52% , $I = 1.79$ and $J = 0.39$.

Fig. 11. The passage of three blades in front of the air duct and changes in the torque diagram.



Table 9. Comparison of the torque and thrust reduction by applying aeration.

Qh	I = 127%				I = 179%			
	J = 0.39		J = 0.6		J = 0.39		J = 0.6	
	Torque	Thrust	Torque	Thrust	Torque	Thrust	Torque	Thrust
13%	13%	13%	9.7%	6.8%	21%	22%	19%	21%
26%	39%	40%	18.7%	15%	40%	44%	35%	37%
38%	49%	49%	29%	26%	48%	51%	37%	40%
52%	54%	55%	34%	31%	51%	55%	45%	47%

When the propeller rotation continues, and the leading edge of the red blade approaches the air duct front, the torque decreases, and the graph becomes downward (from 11 to 36 degrees). At the angle of 36°, the torque value is minimum, and the trailing edge of the yellow blade and the leading edge of the red blade is located at the front area of the duct and are ventilated. A small peak is created from the angle of 36° to 67°, because at the angle of 36° two blades are simultaneously aerating and the torque is minimum, and then the yellow blade exits and the torque increases slightly (at 50°). When the red blade is completely located in the front area of the air duct at an angle of 67°, the torque decreases. Then, as the leading edge of the red blade leaves the front of the air duct, the torque increases again at an angle 85°. When the leading edge of the blue blade approaches the front area of the air duct the torque decreases again. This pattern continues as the trailing edge of the blue blade, and the leading edge of the red blade are both in front area of the duct from 85 to 110 degrees. The torque reaches its minimum at an angle of 110°. This process is repeated for the next blades. In general, the torque values are minimum in two states. State 1: When only one blade is precisely in the front area of the air duct and state 2: When the trailing edge of a blade and the leading edge of the other blade are located at the front area of the air duct. Also, the torque values are maximum in one state, when the leading edge of a blade leaves the front area of the air duct. It is important to note that the angle at which the torque is at its extremum depends on the hydraulic diameter, and these angles change as the hydraulic diameter ratio changes.

The comparisons of average torque, average thrust, and average efficiency in aeration cases for four different values of the hydraulic diameter ratio and without aeration are presented in Fig. 12 and Table 9. The torque and thrust are averaged over one rotation propeller of the propeller.

These comparison studies are carried out for two values of the immersion ratio ($I = 1.27$ and $I = 1.79$), and for two values of the advance coefficient ($J = 0.39$ and $J = 0.6$). In all cases, the results indicate that the increase of hydraulic diameter ratio decreases the average torque and the thrust. But it has no significant effect on the average efficiency, and it is almost constant. Table 9 shows the percentage of torque and thrust reduction in four hydraulic diameters compared to the without aeration state.

In Figs. 13 and 14, the flow patterns around the propeller for the two immersion ratios (i.e., $I = 1.27$ and $I = 1.79$) and the four hydraulic diameter ratios (i.e., 13%, 26%, 38%, and 52%) are shown. Increase in the duct hydraulic diameter causes a more ventilation. The water-air mix is very low in the air duct with a hydraulic diameter ratio of 13% and increases significantly for $Qh = 26\%$. Figure 12, Table 9, Fig. 13, and 14 show that the significant influence on changing the duct diameter is related to the ratio of 13% to 26%, and increasing the duct diameter from the ratio of 38% to 54% does not have much effect on reducing torque and thrust.

By decreasing the immersion ratio, the volume of the water-air mixture increases for all the hydraulic diameter ratios. It can be seen that after the blades impact the water-air mixture, the water-air mixture is cut and thrown forward.

Figure 15 shows the ventilation on the pressure and the suction side of the blade that is located in the air duct area. The ventilation values correspond to a volume fraction of 1, indicating full water fluid (shown in red), and a volume fraction of 0 representing the full air-fluid (shown in blue). In all cases, ventilation occurs on the leading and trailing edges of the blade, and the ventilation volume increases with the increase in the hydraulic diameter ratio. The ventilation length on the leading edge is the highest in the hydraulic diameter ratio of 52%. The trailing edge of the blade close to the air duct area, which passes through the two-phase flow in the front of the duct, is more ventilated. The reason is the thickness of the trailing edge of these types of propellers. As shown in Fig. 16, the air bubbles on this edge collapse after it passes in the front of the air duct.

Figure 17 compares the changes of the advance coefficient and immersion ratio on the torque and thrust in different cases of aeration. The horizontal axis of the diagram shows different aeration cases. Basically, in without aeration case, the torque coefficients decrease while the advance coefficient increases, because of decreasing the pressure on the blades when the inlet velocity of the water is increased.

As shown in Fig. 17, for $I = 1.27$, as the advance coefficient increases from 0.39 to 0.6, the torque coefficient decreases for $Qh = 0$ and 13% but, increases for other hydraulic diameter ratios. This is due to increasing the pressure on the blades while the advance coefficient rises for the hydraulic diameter ratios of 26%, 38%, and 52%. Under neglecting the aeration condition, the torque coefficient decreases as the advance coefficient increasing. Figure 18 presents the pressure coefficient contours for two advance coefficient and the hydraulic diameter ratio of 38%, where the torque coefficient increases as the advance coefficient rises. The contour represents the maximum and minimum pressures in the entire field. Comparing the contours shows the more significant pressure on the propeller for $J = 0.6$.

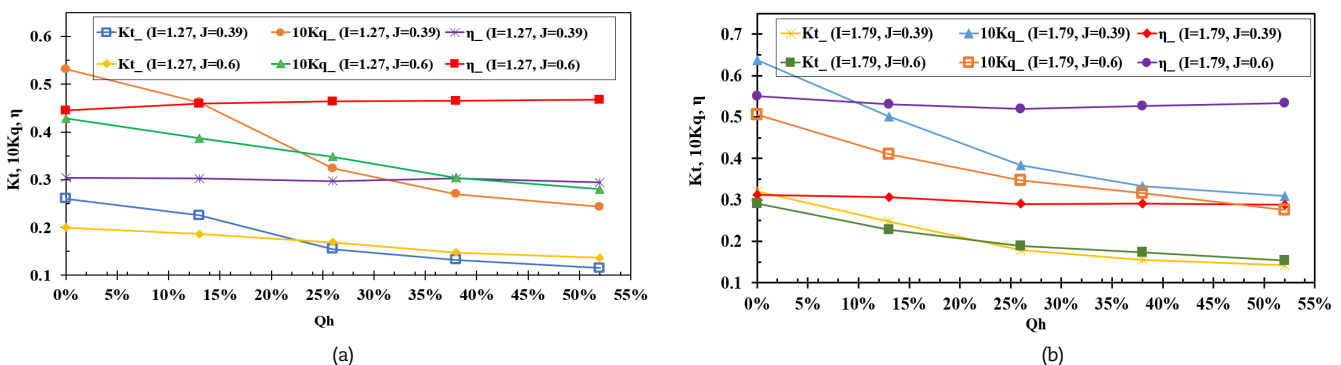


Fig. 12. Variations of the torque, thrust and efficiency for $Qh = 0, 13\%, 26\%, 38\%$ and 52% : (a) $I = 1.27, J = 0.39$ and 0.6 , (b) $I = 1.79, J = 0.39$ and 0.6 .



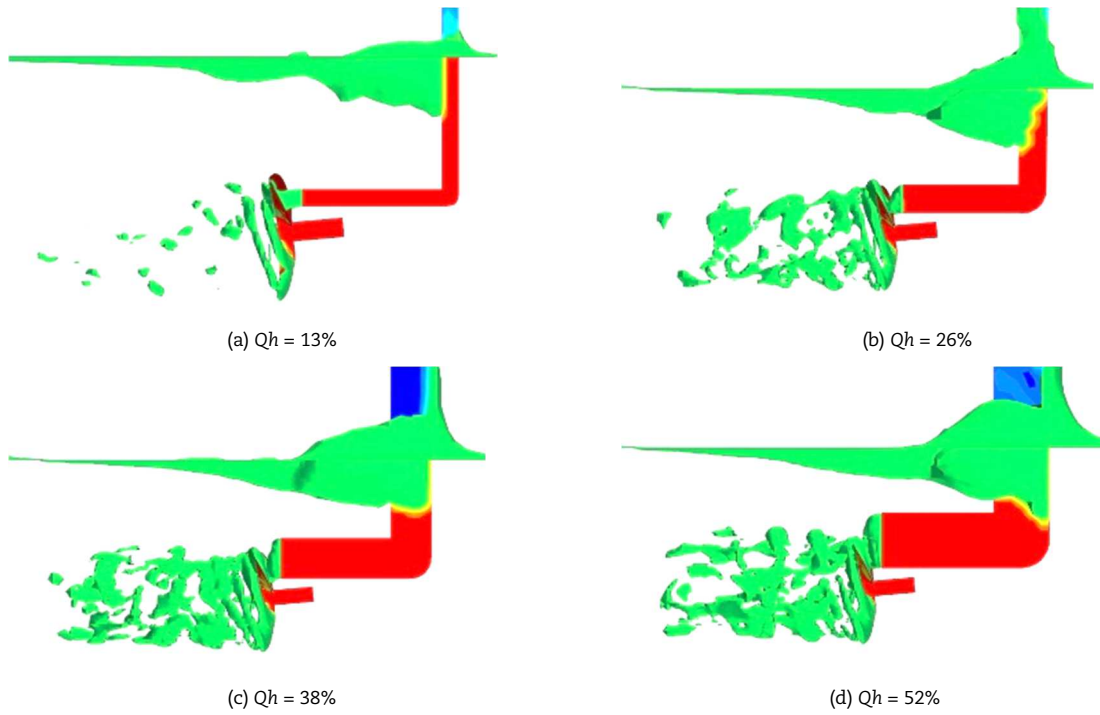


Fig. 13. Two-phase flow around the propeller after 5 rotations in the aeration cases $J = 0.39$ and $I = 1.79$.

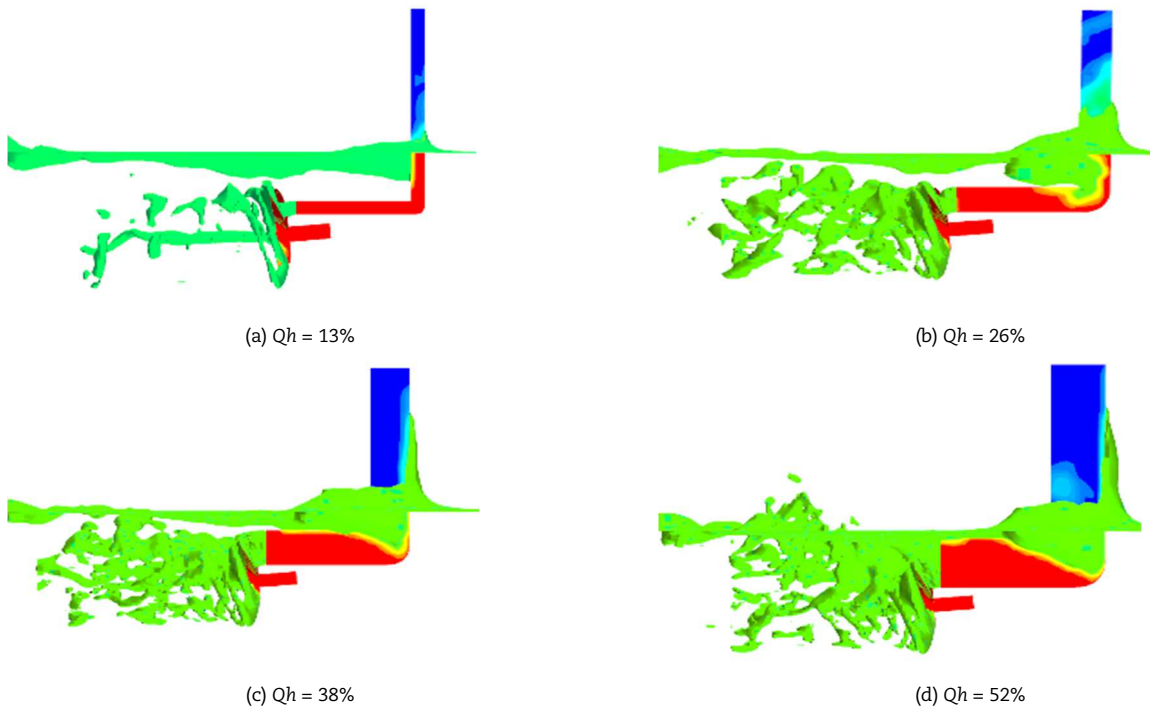


Fig. 14. Two-phase flow around the propeller after 5 rotations in the aeration cases $J = 0.39$ and $I = 1.27$.

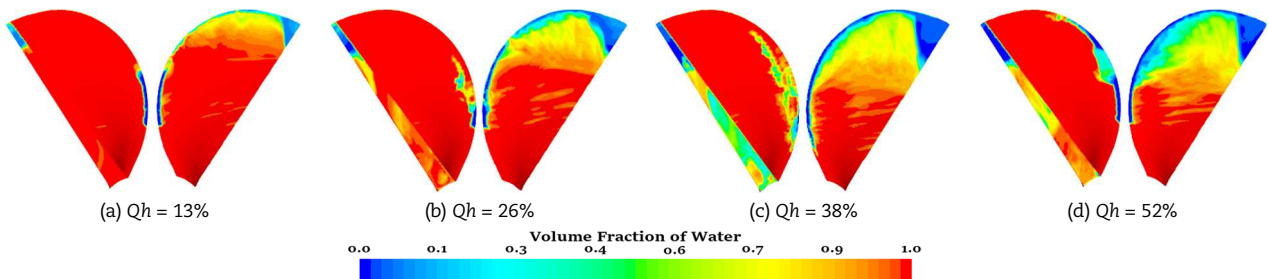


Fig. 15. Ventilation on the pressure side (left figure) and suction side (right figure) at the angle of 326° for the different values of Q_h ($J = 0.39$ and $I = 1.79$).



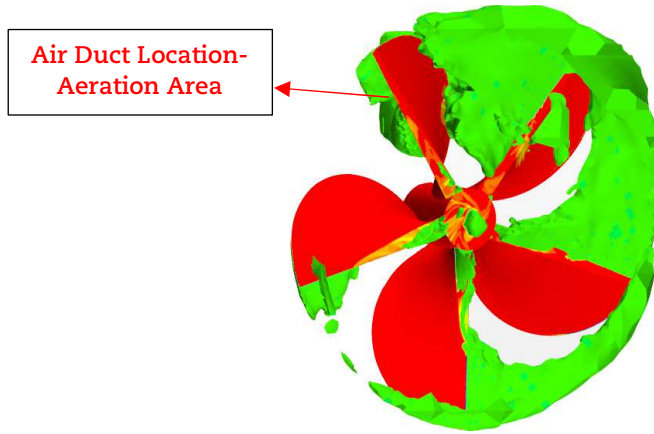


Fig. 16. Pattern of flow on the propeller blades.

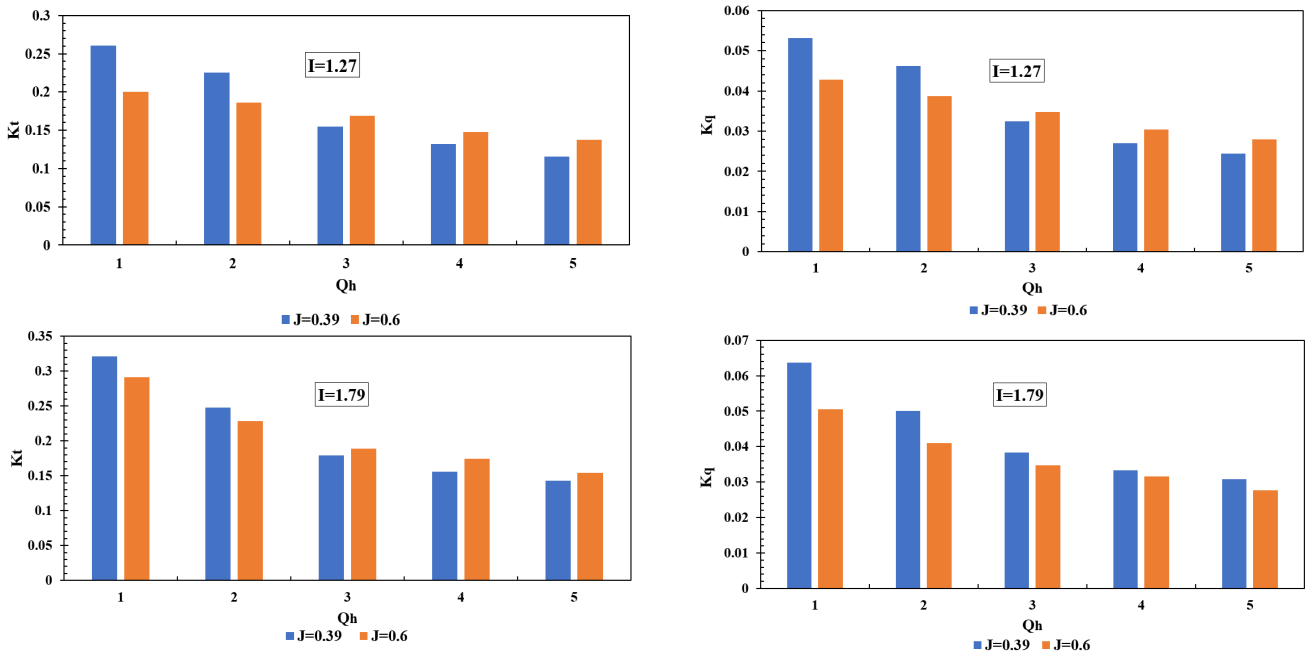


Fig. 17. Comparison of changes of the advance coefficient and immersion ratios on the torque and thrust coefficients.

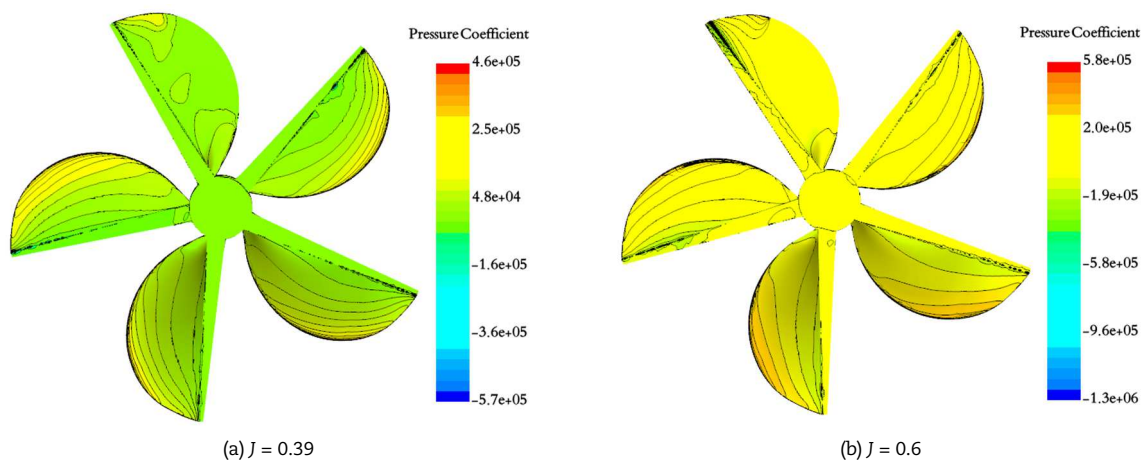


Fig. 18. The pressure contour on the propeller for $I = 1.27$ and $Qh = 38\%$.

For the immersion ratio of $I = 1.79$, by increasing the advance coefficient, the torque decreases in all aeration cases. The ventilation volume cannot prevent the decreasing trend of the torque coefficient. Investigation of the pressure field at this immersion ratio shows that the pressure on the blades continuously decreases with the increase of the advance coefficient.



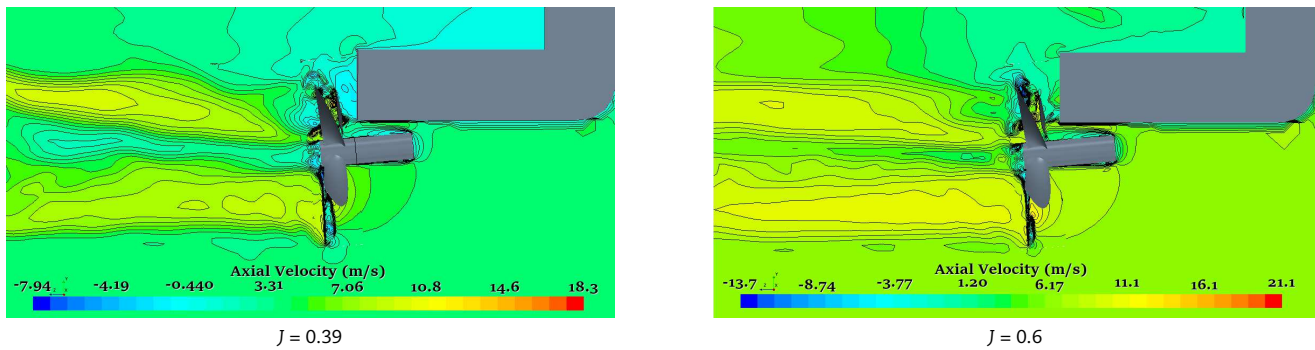


Fig. 19. Axial velocity contour for the hydraulic diameter ratio of 38%.

Basically, in without an aeration state, with the increase of the advance coefficient, the thrust coefficient decreases. The thrust (T) is calculated as:

$$T = m(V_i - V_o) \quad (12)$$

where m is the fluid mass, and V_i and V_o are the inlet and outlet velocity of the fluid, respectively. One of the most important factors in the thrust is the difference between the inlet velocity and accelerated velocity by the propeller. Since at low advance coefficients, the inlet velocity of the flow to the propeller is low, the speed difference becomes large. Therefore, with the increase of the advance coefficient, the thrust coefficient decreases [37]. It can be seen from Fig. 17 that for both considered immersion ratios, the increase of the advance coefficient causes the reduction of thrust coefficient in case of without aeration cases and for $Q_h = 13\%$. But for $Q_h \geq 26\%$, the thrust coefficient increases by increasing the advance coefficient. This is because applying sufficient aeration results in a large difference between the inlet and outlet velocities at the high advance coefficient. This is shown in Fig. 19, which compares the contour of the axial velocity at the immersion ratio of 1.79 and the hydraulic diameter ratio of 38% for two advance coefficients of 0.39 and 0.6. The contour values are drawn for the maximum and minimum velocities in the total field. By comparing both contours, it is found that the difference between the inlet and outlet velocities for the case $J = 0.6$ is greater than the $J = 0.39$.

4. Conclusions

In this study, based on an actual propulsion system of a planing boat, the effects of the square air ducts on the thrust, torque, performance, and ventilation of the surface-piercing propeller were explored. The few related previous works did not fully cover the study requirement of high-speed planing craft, as they did not focus on the actual surface propulsion system arrangement. The fluid flow around the SPP was simulated using the multi-physics computational fluid dynamics software STAR-CCM+ based on the Reynolds-averaged Navier–Stokes equations (RANS). The simulation was validated for grid independence and compared with sea trial results. The effects of the hydraulic diameter of the square air ducts were investigated on the hydrodynamic characteristics of the SPP in the fully submerged position, and the results were compared to the case without aeration. Four air ducts with hydraulic diameter ratios of 13%, 26%, 38%, and 52% were selected. The study was carried out for two immersion ratios of $I = 1.27$ and $I = 1.79$ and two advance coefficients of 0.39 and 0.6. The findings included:

- Increasing the duct hydraulic diameter and consequently increasing the aeration to the propeller, the torque and thrust decrease significantly, while the efficiencies in different aeration cases remained almost constant.
- In all cases studies, the aeration has the most negligible effect on the torque and thrust for the hydraulic diameter ratio of $Q_h = 13\%$, but at 26%, the torque and thrust coefficients decrease significantly. At 38%, the reduction rate of the torque and thrust drops, and for 52%, this rate in comparison to the previous cases is not significant.
- Applying aeration resulted in oscillations with large and small peaks in the torque and thrust diagram. The large peak corresponds to the leaving of the leading edge of the blade from the air duct area. Also, the small peak occurs when the leading edge of a blade and the trailing edge of the next blade are exposed to aeration and then, the second blade is exited from the front area of the air duct entirely.
- The propeller experiences partial ventilation, and the leading and trailing edges are ventilated. The trailing edge of the blades that are near the air duct and pass the two-phase flow are more ventilated, and by the propeller rotation and moving away from the duct, the air bubbles collapse, and the ventilation volume decreases. The maximum ventilation occurs on the suction side of the propeller and at the lower advance coefficient.
- In two cases of the without aeration and the hydraulic diameter ratio of 13% and for the immersion ratio of $I = 1.27$, by the increase of the advance coefficient from 0.39 to 0.6, the torque coefficient decreases. But it increases for $Q_h \geq 26\%$. At the immersion ratio of $I = 1.79$, in all aeration cases, by the increase of the advance coefficient, the torque coefficient continuously decreases, and the ventilation volume cannot change the reduction rate of the torque coefficient.
- For both considered immersion ratios, the thrust coefficient decreases by increasing the advance coefficient for $Q_h = 13\%$ and the case of without aeration. However, for $Q_h \geq 26\%$, when increasing the advance coefficient, the thrust coefficient increases.
- A larger duct clearly increases boat resistance and affects the inlet flow to the propeller. Additionally, due to the significant impact of the hydraulic diameter ratio of 26% on the torque and thrust reduction, this hydraulic diameter ratio is recommended for aeration with the square duct.

Author Contributions

M.P. Bushehri conducted the numerical simulation and sea trials and analyzed the results; M.R. Golbahar Haghighi planned the scheme, initiated the project, and suggested the numerical simulation and experiments; P. Malekzadeh and E. Bahmyari suggested the governing equations, the modeling of numerical simulation, the sea trial and the validation method. The manuscript was written through the contribution of all authors. All authors discussed the results, reviewed, and approved the final version of the manuscript.



Acknowledgments

This research did not receive any specific grant from funding agencies in the public, commercial, or not-for-profit sectors

Conflict of Interest

The authors declared no potential conflicts of interest concerning the research, authorship, and publication of this article.

Funding

The authors received no financial support for the research, authorship, and publication of this article.

Data Availability Statements

The datasets generated and analyzed during the current study are available from the corresponding author on reasonable request.

Nomenclature

D_h	Hydraulic diameter (m)	T	Thrust (kN)
D	Propeller diameter (m)	t	Time (s)
DAR	Developed area ratio	V	Velocity (ms^{-1})
I	Immersion ratio	V_a	Advance speed (knots, ms^{-1})
J	Advance coefficient	V_i	Velocity inlet (ms^{-1})
K	Turbulent kinetic energy (J/kg)	V_o	Velocity outlet (ms^{-1})
K_q	Torque coefficient	V_s	Ship speed (knots, ms^{-1})
K_t	Thrust coefficient	μ	Dynamic viscosity (N.s/m^2)
L	Length (m)	μ_t	Turbulent viscosity (N.s/m^2)
n_{prop}	Propeller speed (rpm, rps)	ρ	Density (kg/m^3)
p	Pressure (Pa)	U	Velocity component
q	Torque (N.m)	\bar{S}_{ij}	Mean strain rate tensor components
Q_h	Hydraulic diameter ratio	ε	Turbulent dissipation rate
R_t	Total resistance (kN)		

References

- [1] Shiba, H., Air-drawing of marine propellers, *Report of Transportation Technical Research Institute*, 9, 1953, 1-320.
- [2] Hadler, J., Performance of partially submerged propellers, *7th ONR Symposium on Naval Hydrodynamics-Rome*, August, 1968.
- [3] Hecker, R., Experimental performance of a partially submerged propeller in inclined flow, *Society of Naval Architects and Marine Engineers*, 1973.
- [4] Rains, D.A., Semi-submerged propellers for monohull displacement ships, *In SNAME Propeller and Shafting Symposium*, 1981.
- [5] Rose, J.C., Kruppa, C., *Methodical series model test results*, 1991.
- [6] Kruppa, C., *Testing surface piercing propellers*, 1992.
- [7] Olofsson, N., *Force and flow characteristics of a partially submerged propeller*, Ph.D. Thesis, Chalmers University of Technology, 1996.
- [8] Young, Y.L., Kinnas, S.A., Analysis of super cavitating and surface-piercing propeller flows via BEM, *Computational Mechanics*, 32(4-6), 2003, 269-280
- [9] Kinnas, S.A., Young, Y.L., Modeling of cavitating or ventilated flows using BEM, *International Journal of Numerical Methods for Heat & Fluid Flow*, 13(6), 2003, 672-697.
- [10] Ghassemi, H., Shademani, R., Ardeshir, A., Hydrodynamic characteristics of the surface-piercing propeller for the planing craft, *In International Conference on Offshore Mechanics and Arctic Engineering*, 2009.
- [11] Yari, E., Ghassemi, H., Numerical analysis of surface piercing propeller in unsteady conditions and cupped effect on ventilation pattern of blade cross-section, *Journal of Marine Science and Technology*, 21, 2016, 501-516.
- [12] Caponnetto, M., RANSE simulations of surface piercing propellers, *In Proceedings of the 6th Numerical Towing Tank Symposium*, Rome, Italy, 2003.
- [13] Califano, A., Steen, S., Identification of ventilation regimes of a marine propeller by means of dynamic-loads analysis, *Ocean Engineering*, 38(14-15), 2011, 1600-1610.
- [14] Himei, K., Numerical analysis of unsteady open water characteristics of surface piercing propeller, *In Third International Symposium on Marine Propulsors smp*, 2013.
- [15] Yu-xiang, S., Ling-xin, Z., Xue-ming, S., Numerical study of the hydrodynamic performances of surface piercing propeller, *Journal of Mechanical & Electrical Engineering*, 31(8), 2014, 985-990.
- [16] Yari, E., Ghassemi, H., The unsteady hydrodynamic characteristics of a partial submerged propeller via a RANS solver, *Journal of Marine Engineering & Technology*, 14(3), 2015, 111-123.
- [17] Alimirzazadeh, S., Roshan, S.Z., Seif, M.S., Unsteady RANS simulation of a surface piercing propeller in oblique flow, *Applied Ocean Research*, 56, 2016, 79-91.
- [18] Javanmardi, N., Ghadimi, P., Hydroelastic analysis of a semi-submerged propeller using simultaneous solution of Reynolds-averaged Navier-Stokes equations and linear elasticity equations, *Proceedings of the Institution of Mechanical Engineers, Part M: Journal of Engineering for the Maritime Environment*, 232(2), 2018, 199-211.
- [19] Rad, R.G., Shafaghat, R., Yousefi, R., Numerical investigation of the immersion ratio effects on ventilation phenomenon and also the performance of a surface piercing propeller, *Applied Ocean Research*, 89, 2019, 251-260.
- [20] Nouroozi, H., Zeraatgar, H., A reliable simulation for hydrodynamic performance prediction of surface-piercing propellers using URANS method, *Applied Ocean Research*, 92, 2019, 101939.
- [21] Seyyedi, S.M., Shafaghat, R., Siavoshian, M., Experimental study of immersion ratio and shaft inclination angle in the performance of a surface-piercing propeller, *Mechanical Sciences*, 10(1), 2019, 153-167.
- [22] Seyyedi, S.M. Shafaghat, R., A review on the Surface-Piercing Propeller: Challenges and opportunities, *Proceedings of the Institution of Mechanical Engineers, Part M: Journal of Engineering for the Maritime Environment*, 234(4), 2020, 743-770.
- [23] Pakian Bushehri, M., Golbahar Haghighi, M.R., Experimental and numerical analysis of Hydrodynamic Characteristics of a surface piercing propeller mounted on high-speed craft, *International Journal of Maritime Technology*, 15, 2021, 79-91.
- [24] Yari, E., Moghadam, A.B., BEM applied to the cup effect on the partially submerged propeller performance prediction and ventilation pattern, *Journal*




of *Marine Engineering & Technology*, 21(3), 2022, 159-177.


- [25] Kamran, M., Nouri, N., Askarpour, H., Numerical Investigation of the Effect of Trailing Edge Shape on Surface-Piercing Propeller Performance, *Applied Ocean Research*, 125, 2022, 103230.
- [26] Seif, M.S., Teimouri, M., The study on the scaling effects in the surface piercing propeller, *Ocean Engineering*, 267, 2023, 113156.
- [27] Bushehri, M.P., Haghghi, M.G., Propulsion System Matching Analysis of a Catamaran Passenger Ship by Changing the Gear Ratio, *Iranian Journal of Science and Technology, Transactions of Mechanical Engineering*, 47(1), 2022, 91-107.
- [28] Yang, D., Numerical analysis on the hydrodynamic performance of an artificially ventilated surface-piercing propeller, *Water*, 10(11), 2018, 1499.
- [29] Gao, Z., Numerical analysis on the effect of artificial ventilated pipe diameter on hydrodynamic performance of a surface-piercing propeller, *Journal of Marine Science and Engineering*, 7(8), 2019, 240.
- [30] Amini, A., Nouri, N.M., Abedi, A., Kamran, M., Performance improvement of surface piercing propeller at low advance coefficients by aeration, *Ocean Engineering*, 238, 2021, 109551.
- [31] Amini, A., Nouri, N.M., Niazi, S., Abedi, A., A Numerical Study on Surface-piercing Propellers using Sliding Mesh Method via Openfoam Software, *Iranica Journal of Energy & Environment*, 14(4), 2023, 415-22.
- [32] Wheeler, M.P., Matveev, K.I., Numerical Modeling of Surface-Piercing Flexible Hydrofoils in Waves, *Journal of Ship Research*, 67(02), 2023, 140-9.
- [33] Matveev, K.I., Wheeler, M.P., Xing, T., Numerical simulation of air ventilation and its suppression on inclined surface-piercing hydrofoils, *Ocean Engineering*, 175, 2019, 251-61.
- [34] Molland, A.F., Turnock, S.R., Hudson, D.A., *Ship resistance and propulsion*, Cambridge University Press, 2019.
- [35] Javanmard, E., Yari, E., Mehr, J.A., Mansoorzadeh, S., Hydrodynamic characteristic curves and behavior of flow around a surface-piercing propeller using computational fluid dynamics based on FVM, *Ocean Engineering*, 192, 2019, 106445.
- [36] CD-adapco, G., *STAR-CCM User Guide Version 9.06*, C.-a. Group, Editor, NY, USA, 2014.
- [37] Husaini, M., Samad, Z., Arshad, M.R., *Autonomous underwater vehicle propeller simulation using computational fluid dynamic*, In: *Computational Fluid Dynamics Technologies and Applications*, IntechOpen, 2011.

ORCID iD

Mojtaba Pakian Bushehri  <https://orcid.org/0009-0009-8798-2396>

Mohammad Reza Golbahar Haghghi  <https://orcid.org/0000-0002-5157-566x>

Parviz Malekzadeh  <https://orcid.org/0000-0003-1033-6395>

Ehsan Bahmyari  <https://orcid.org/0000-0002-8202-8124>



© 2024 Shahid Chamran University of Ahvaz, Ahvaz, Iran. This article is an open access article distributed under the terms and conditions of the Creative Commons Attribution-NonCommercial 4.0 International (CC BY-NC 4.0 license) (<http://creativecommons.org/licenses/by-nc/4.0/>).

How to cite this article: Bushehri M.P., Golbahar Haghghi M.R., Malekzadeh P., Bahmyari E. Investigating the Effects of Air Duct Dimensions on Aeration and Hydrodynamic Characteristics of a Surface-piercing Propeller, *J. Appl. Comput. Mech.*, 10(2), 2024, 392-405. <https://doi.org/10.22055/jacm.2024.45072.4308>

Publisher's Note Shahid Chamran University of Ahvaz remains neutral with regard to jurisdictional claims in published maps and institutional affiliations.

